Journal of Fluids and Structures 137 (2025) 104379

Contents lists available at ScienceDirect

Journal of Fluids and Structures

journal homepage: www.elsevier.com/locate/jfs

Compound-channel-driven shear layer impinging upon streamwise-oriented plates of different solidities

Victor Dupuis [a],[*], Guillaume Bonduelle [a,b], Olivier Eiff [a]

[a] Institut für Wasser und Umwelt, Karlsruher Institut für Technologie, Kaiserstraße 12, Karlsruhe 76131, Germany
[b] Institut National Polytechnique de Toulouse, 6 allée Emile Monso, Toulouse 31029, France

ARTICLE INFO

Keywords:
Shear layer
Large-scale structures
Compound channel
Turbulence control

ABSTRACT

The impingement of a compound open-channel flow upon vertical and streamwise-oriented plates of different solidities located at the edge between main channel and floodplain are investigated experimentally. The plates model finite-length thin hedges along the river bank. The incident flow is characterised by a turbulent shear layer dominated by Kelvin–Helmholtz structures of length L_s. The solidity of the plates is varied from 17% (i.e. 83% porosity) to 100% (solid plate) in order to represent different vegetation densities, while the plate length is fixed to $0.56L_s$. The velocity field at the free-surface is measured by means of Large-Scale Particle Image Velocimetry (LS-PIV) with a field of view of length $3L_s$ and covering the channel width. While the solid plate is shown to induce a significant decrease in the incoming turbulent shear stress, the porous plates instead lead to an overshoot in the turbulent shear stress. All plates induce a reduction of the lateral turbulence intensity, while the longitudinal turbulence intensity is never reduced and even strongly overshoots the incident value for the porous plates. The individual Kelvin–Helmholtz structures are altered when passing the plates but are not destroyed. The alteration of the structures increases with the plates' solidity, but the vortex cores as well as their spatial periodicity are always maintained, and the structures reform to their original state within a relatively short distance downstream of the plates of about $1.5L_s$. While for the solid plate the vorticity within the vortex cores decreases by the passage of the plate, in the case of the porous plates the vorticity increases. Vorticity shed from the holes of the porous plates is surmised to be the cause of this increase. The ensemble-averaged Kelvin–Helmholtz structure downstream of each plate reveals that for the least solid plates, the upstream ejection associated with the vortex core is strongly strengthened, which accounts for the observed overshoots in the turbulent stresses. When the plate's solidity is higher than 67% however, the Kelvin–Helmholtz vortex downstream of the plate has shrunk and weakened, but is accompanied by secondary vortices, generated by the interaction with the plates.

1. Introduction

When rivers overflow the main channel into the floodplain, the flow cross-section takes the form of what is commonly referred to as a compound section with a deep main channel and adjacent shallow floodplains. Due to the generally strong velocity differences between these sub-sections, a turbulent shear layer develops at the interface between main channel and floodplain, which increases energy loss as compared to the case when main channel and floodplain were non-interacting (Myers et al., 2001). Moreover, under

---

[*] Corresponding author.
E-mail address: victor.dupuis@kit.edu (V. Dupuis).

https://doi.org/10.1016/j.jfluidstructs.2025.104379
Received 27 August 2024; Received in revised form 17 April 2025; Accepted 30 June 2025

the condition that the shear parameter $\lambda = (U_2 - U_1)/(U_2 + U_1)$ – where U_1 and U_2 are the velocities beyond the shear layer, on the low-speed and high-speed side respectively – is higher than a critical value $\lambda_c \approx 0.3$, large-scale structures of Kelvin–Helmholtz type develop in the shear layer (Proust et al., 2017; Dupuis et al., 2023b). These large-scale structures span the whole water column in the floodplain (Dupuis et al., 2017) and contribute largely to the turbulence of the shear layer (Dupuis et al., 2023a). They also play a role for river ecology, as large-scale structures increase the lateral mixing of dissolved nutriments and pollutants as well as suspended matter and debris (Bouchez et al., 2010).

In order to more reliably predict the flow conveyance capacity of a compound channel, the roughness and especially the vegetation present on the floodplain has to be accounted for. The focus herein will be set on vegetation located at the edge between floodplain and main channel, in particular hedges, which are often present along floodplain edges.

A row of trees at the floodplain edge was found to increase the turbulence at the main channel/floodplain interface (Fernandes et al., 2018) and to increase the global channel friction coefficient (Branß and Aberle, 2022), leading to a reduced channel conveyance (Sun and Shiono, 2009). The channel conveyance is increased only for a very dense row of trees at the floodplain edge, since the dense row isolates the main channel from the floodplain (Terrier et al., 2010).

The aforementioned studies only investigated the impact of a continuous row of trees along the floodplain edge, and therefore considered streamwise-uniform flows. By contrast, the flow non-uniformity and local disturbance of the shear layer due to an isolated element at the floodplain edge was only scarcely investigated so far, although it is a common situation in the field. Gymnopoulos et al. (2019) studied the forces on a single emergent cylinder set at the floodplain edge, but without investigating the impact of the cylinder on the shear layer turbulence. They showed that the drag coefficient of the cylinder is slightly lower as compared to the case when the incident flow is not sheared and that the cylinder is subjected to a mean lateral lift force, directed towards the floodplain.

The present study aims at investigating thin and finite-length vegetation hedges of different densities at the floodplain edge, focusing on the impingement of the shear layer upon the hedges. Such hedges are conceptually close to streamwise-oriented plates of different solidities.

Finite-length streamwise-oriented solid plates in turbulent flows were so far investigated in the context of Large-Eddy Break-Up devices (LEBU), also referred to as outer-layer manipulators. These devices are placed in turbulent boundary layers in order to reduce surface drag. A thin plate is set parallel to the wall and its interaction with the turbulent structures of the boundary layer is found to induce a reduction of wall friction downstream of the plate. The optimal design for reducing the surface drag with a single (solid) plate was found to be a thin plate of length on the order of the boundary layer thickness δ, set at a distance of around 0.75δ from the wall (Dowling, 1985). An alternative design is the tandem configuration with two plates each of length δ and separated by a streamwise distance of about 10δ (Cousteix et al., 1989; Guezennec and Nagib, 1990). A maximum local skin-friction reduction at the wall on the order of 30% can be reached. Yet, a net drag reduction can only be achieved if the drag of the device itself is low. This implies using tensioned ribbons, with which a maximum net drag reduction on the order of 6% over a distance of 100δ can be achieved (Savill and Mumford, 1988; Iuso and Onorato, 1995). The drag reduction is found to be related to the reduction of turbulence near the wall (Savill and Mumford, 1988). LEBUs were also shown to reduce the strength of incoming vortices (Swirydczuk et al., 1993) and to reduce overall the turbulent length scales (Chan et al., 2022).

When the streamwise-oriented plate is replaced by a cylinder of same drag, the efficiency of the LEBU is drastically reduced and no net drag reduction is observed (Savill and Mumford, 1988). This is in accordance with the above mentioned fact that rows of trees (modelled by cylinders) along the floodplain edge induce an increase in flow resistance rather than a decrease, and are therefore disadvantageous for the flow conveyance capacity of the channel. The LEBU studies, on the other hand, suggest that the effect may be different with thin hedges, conceptually closer to streamwise-oriented plates.

In the context of modelling a leafy vegetation patch in an open-channel flow, we showed in Dupuis et al. (2023c) that thin vertical streamwise-oriented plates in a patch configuration are very effective in reducing turbulence in an open-channel flow. Contrary to LEBUs, the plates were positioned normal to the channel bottom. The patch achieved a reduction of 85% of the turbulent shear stress, whereas the longitudinal and vertical turbulent normal stresses were reduced by 50% and 80% respectively. In addition, the patch affected only slightly the time-averaged velocity field, the velocity drop in the wake being very weak or even close to non-existent, suggesting a very low induced drag.

In the present study, the hedges at the floodplain edge are modelled by streamwise-oriented plates of different solidities. The main purpose is to investigate the potential turbulence-reduction effect of these idealised hedges. To this end, the thickness of the plates is kept very small in order to minimise the self-induced turbulence due to the plates' wake and thus to better highlight the potential turbulence reduction of the incoming flow. The plates' thickness is therefore not representative of real hedges. The effect of the hedge thickness and the inner flow through the hedge should be treated in a separate study.

The first objective of the present study is to assess the effect of plates of different porosities on the turbulence of a compound-channel-driven shear layer. Does the plates, in this flow and geometric configuration, reduce the incident turbulence, as it does in the case of LEBUs in a boundary layer? A second objective is to observe how the individual incident large-scale Kelvin–Helmholtz structures are affected by their impingement upon the plates of different porosities.

In order to address these issues, an experimental study was carried out by installing emergent vertical plates near the floodplain edge of a compound channel, where the turbulent shear stress of the shear layer is maximum. The length of the plates was set constant since the focus is to examine the effect of solidity of the plates in order to model vegetation hedges of different densities. The plate solidity was varied from 17% (i.e. 83% porosity) to 100% (solid plate). The incident flow is close to one of the flows investigated in Dupuis et al. (2023b) and is dominated by quasi-periodic Kelvin–Helmholtz large-scale structures of typical length $L_s = 0.9\,\mathrm{m}$. The choice of the length of the plate was based on our previous work in Dupuis et al. (2023c), where we proposed a

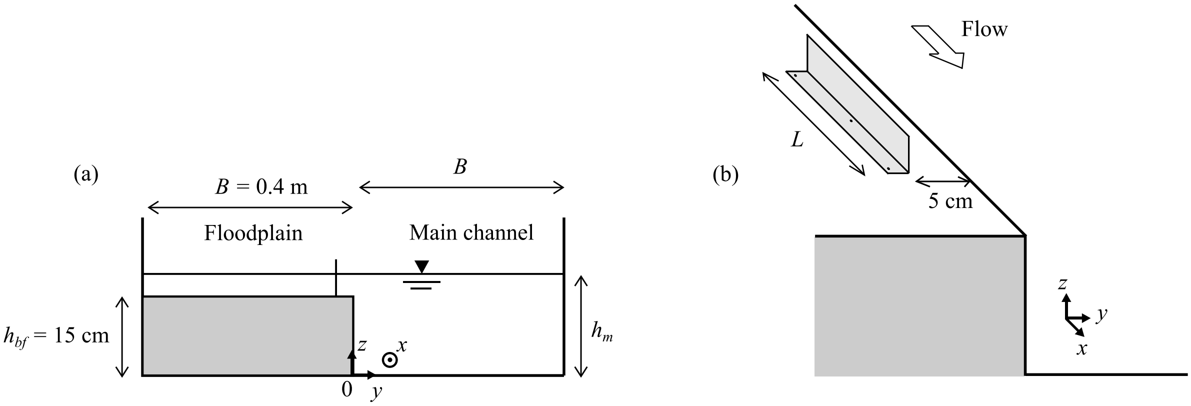

Fig. 1. (a) Channel cross-section (view from downstream), (b) location of the plates on the floodplain bottom.

non-dimensional number to characterise the efficiency of a solid streamwise-oriented plate to destroy a vortical structure of a given size. It was based on the assumption that the turbulence reduction induced by a streamwise-oriented plate is due to the lateral impingement of the plate-normal fluctuating movements against the plate, in analogy to the turbulence reduction mechanisms assumed for honeycombs (Loehrke and Nagib, 1976). The number therefore compares the turnover time of a vortical structure to the advection time past the plate, and is defined by:

$$E = \frac{L}{U_c}\frac{u_r}{d} \tag{1}$$

where L is the length of the plate, d the size of the incoming vortical structure, u_r the velocity fluctuation induced by the vortical structure and U_c the convection velocity of the structure. In Dupuis et al. (2023c), only a very rough estimate of $E \approx 0.6$ could be given for the plate to be effective in destroying a vortex. A more realistic estimate for the optimal length can be deduced from the optimal LEBU length, which was found to be $L \approx \delta$. Considering that for the LEBU the incoming structures are also on the order of δ, the E-number reduces to the turbulence intensity $E \approx u_{\mathrm{rms}}/U$, which can be roughly estimated at 0.1 for a turbulent boundary layer. We therefore chose a E-number close to 0.1 (see Section 2).

A large-scale PIV set-up, described in Section 2, was implemented to measure the flow at the free-surface around the plates. The measurement field covers the incident flow, the flow around the plate and about $2L_s$ of the plates' wake. The presentation of the results (Section 3) is organised as follows. First, the characteristics of the incident flow are presented. Then, the impact of the plates on the different turbulent stresses is analysed, followed by the velocity deficit induced in the plates' wake. Next, the ability of the plates to alter the spatial correlation of the incident flow is assessed. The effect of the plates on the Kelvin–Helmholtz structures is then investigated, first by tracking the Kelvin–Helmholtz vortex cores when they pass the plates and then by carrying out an ensemble-average of the Kelvin–Helmholtz structures in the plates' near wake. Finally, a comparison with LEBUs is proposed (Section 4).

2. Experimental method

The experiments were conducted in a 20 m long open-channel flume of width $2B = 80$ cm. A two-stage compound channel geometry was achieved by means of a floodplain made of PVC, with a bankfull level of the main channel of $h_{bf} = 15$ cm, as sketched in Fig. 1a. At the channel entrance on the floodplain side, a ramp of length 1.3 m raises the flow to the bankfull level (see Fig. 3). A splitter plate separates the main channel and the floodplain over 1.45 m from the start of the ramp. On the floodplain side, a grid with an opening of 10% was placed in the cross-section in order to reduce the initial floodplain discharge and in this manner to shorten the development towards flow equilibrium.

The origin of the longitudinal coordinate x is defined at the splitter plate trailing edge. The lateral coordinate y has its origin at the interface between main channel and floodplain and is positive into the main channel. The origin of the vertical coordinate z is at the main channel bottom. The velocities in the corresponding three directions are noted u, v and w. A prime (') indicates the fluctuating part of the instantaneous velocity and an overbar the time-average operator.

A reference flow (S0) without plate and four flows with plates of different solidities and with the same flow conditions as the reference flow were measured. The flow conditions are given in Table 1. The water depth in the main channel is $h_m = 164$ mm and in the floodplain $h_f = h_m - h_{bf} = 14$ mm. The discharge is $Q = 25.8\,\mathrm{L.s^{-1}}$ and the channel slope $S_0 = 0.34\,\mathrm{mm.m^{-1}}$. The bulk velocity of the channel is $U_Q = Q/A = 36.2\,\mathrm{cm.s^{-1}}$, where A is the cross-sectional area. The resulting channel Reynolds number is $Re_Q = U_Q R_h/\nu = 22900$, where R_h is the hydraulic radius and ν the kinematic viscosity. The shear parameter $\lambda = (U_2 - U_1)/(U_2 + U_1)$ was calculated from the lateral profiles of the time-averaged longitudinal velocity at the free surface $\bar{u}(y)$ (see Fig. 4a), taking for U_2 the maximum velocity in the main channel and for U_1 the velocity at the (stable) inflection point in the floodplain. The resulting shear parameter is $\lambda = 0.55$, much above the critical value $\lambda_c = 0.3$ (Proust et al., 2017), such that large-scale Kelvin–Helmholtz

Table 1
Flow conditions for all cases examined: water depth in the main channel h_m and in the floodplain h_f, total discharge Q, slope S_0, bulk velocity U_Q, Reynolds-number Re_Q, shear parameter λ and mean length of the incident Kelvin–Helmholtz structures L_s.

h_m (mm)	h_f (mm)	Q (L.s^{-1})	S_0 (mm m^{-1})	U_Q (cm s^{-1})	Re$_Q$	λ	L_s (m)
164	14	25.8	0.34	36.2	22 900	0.55	0.9

Table 2
Plate characteristics for the different flow cases: solidity S, plate thickness e and plate type.

Flow case	S (%)	e (mm)	Plate type
S0	0	0	none
S17	17	2	wire mesh (wire ∅ 1 mm)
S33	33	1.6	perforated plate (square openings)
S67	67	1.1	perforated plate (round openings)
S100	100	0.7	smooth solid plate

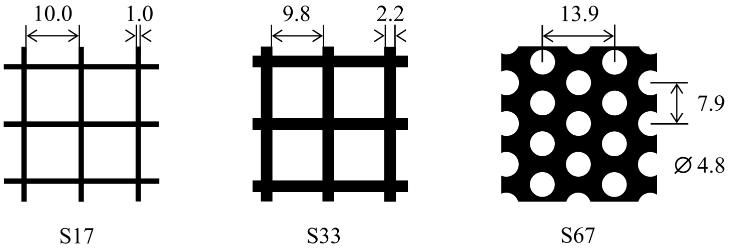

Fig. 2. Geometry of the porous plates with solidity $S = 17$, 33 and 67% (to scale). The lengths are given in mm.

structures are present. The mean length of the Kelvin–Helmholtz structures as determined by spatial correlation (see Section 3.4) is $L_s = 0.9\,\text{m}$.

The plate characteristics of the five flow cases are reported in Table 2. Flow case S0 is the reference flow without plate. For the four other cases, different plates of same length $L = 0.5\,\text{m}$ and of different solidities are fixed on the floodplain bottom. As discussed in the Introduction, the choice of the plates' length was based on a E-number (Eq. (1)) of about 0.1. Taking for the convection velocity $U_c = 19\,\text{cm.s}^{-1}$ (determined below in Section 3.5), for the structures' length $d = L_s = 0.9\,\text{m}$, and for the velocity fluctuation $u_r = \text{rms}(u) = 4\,\text{cm.s}^{-1}$ in the middle of the undisturbed shear layer, Eq. (1) yields $E = 0.12$. This corresponds to a ratio between plate length and length of the incoming structures of $L/L_s = 0.56$. The plates are normal to the bottom, parallel to the x-axis and emergent. They are screwed on the floodplain by bending the plates 90° with a base of 3 cm width, as depicted in Fig. 1b. The plates were positioned laterally at $y = -5\,\text{cm}$, i.e. close to the position where the turbulent shear stress of the reference flow is maximum. The leading edge of the plate is at $x = 9.07\,\text{m}$. The first letter S in the names of the cases stands for *solidity* and is followed by the value of the plate solidity (solid area over total area). The plate with $S = 17\,\%$ is a wire mesh with a wire diameter of 1 mm. The plates with $S = 33$ and 67% are perforated plates with square and round openings respectively. The plate with $S = 100\,\%$ is a smooth solid plate. The thicknesses e of the plates are reported in Table 2 and the geometry of the three porous plates is depicted in Fig. 2.

The velocity field at the free surface was measured by means of a Large-Scale Particle Image Velocimetry set-up (LS-PIV), described in Fig. 3. The free surface is seeded with floating particles made of square pieces of polypropylene foil of side 2.5 mm. Two synchronised cameras (IDS UI-3180CP of resolution $2592 \times 2048\,\text{px}^2$) with 24 mm lenses (Sigma 24/1.8 EX DG Macro) are installed 2.5 m above the water surface, covering together a streamwise distance of 2.7 m ($8.5\,\text{m} < x < 11.2\,\text{m}$) and capturing the whole channel width. The fields of view of the cameras have 9 cm overlap. The free surface is illuminated with two halogen projectors, placed respectively downstream and upstream of the measurement section. The particles are seeded manually at $x \approx 0.4\,\text{m}$ and are collected in a net at $x = 17.4\,\text{m}$. The recording frequency of the cameras was 70 Hz and the measurement time approximately 200 s for each flow case. More detailed informations on the LS-PIV set-up can be found in Dupuis et al. (2023b).

The images were processed with the software Davis10 (LaVision). As the images sometimes featured regions with no or not enough particles, an adaptive mask program (a specific mask for each image) was implemented in Matlab, based on an erosion filter, in order to remove these regions from the processing and from the final velocity field. The final box size of the multi-pass processing was $64 \times 64\,\text{px}^2$ with an overlap of 50%, leading to a spatial resolution of 17.4 mm both in x- and y-directions. Note that this resolution was too coarse to resolve the flow through the pores of the porous plates (cases S17, S33 and S67). The flow at the free surface is expected to be representative of the flow below, since the large-scale turbulent fluctuations of the compound channel shear layer are coherent over the water depth (Dupuis et al., 2017, 2023a). However, one cannot exclude that the interaction between the shear layer and the plates become three-dimensional, at least at scales smaller than the scale of the Kelvin–Helmholtz structures.

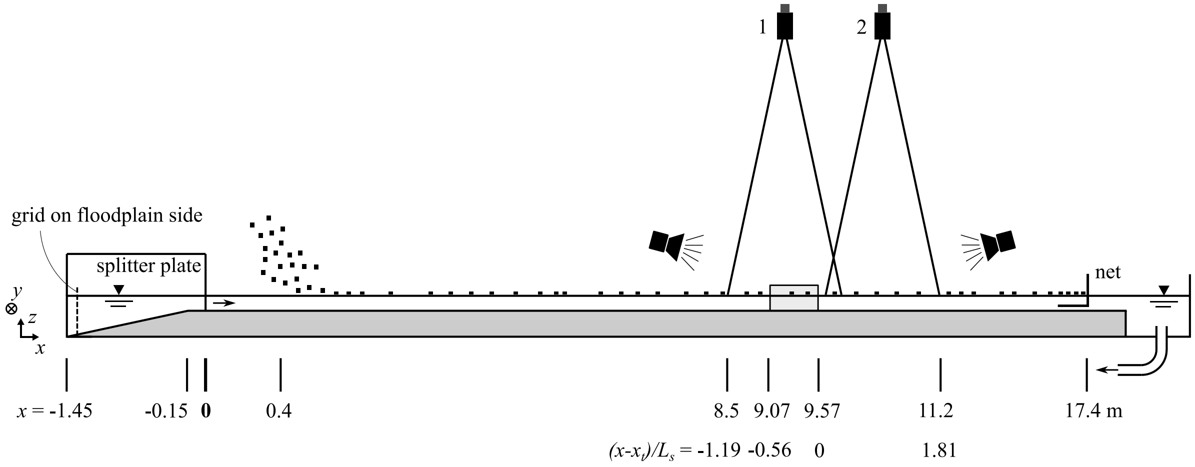

Fig. 3. Sketch of the LS-PIV set-up (not to scale). Both the absolute streamwise coordinate x and the relative normalised streamwise coordinate $(x - x_t)/L_s$ are depicted.

Throughout the paper, we use a normalised streamwise coordinate $(x - x_t)/L_s$ (the mean structures' length L_s being considered to be the most characteristic length scale for the interaction of the incident flow with the plates) which origin is set at the plates' trailing edge at $x_t = 9.57$ m. The lateral coordinate y is normalised by the channel half-width B to easily situate the channel's borders.

3. Results

3.1. Incident flow

Fig. 4 shows lateral profiles of different flow quantities, spatially averaged between $(x-x_t)/L_s = -1.08$ and -0.80, for the reference flow S0. These profiles are representative for the incident flow of all flow cases, although small and non-significant variations were present. The mean velocity $\overline{u}(y)$ (Fig. 4a) exhibits a profile of hyperbolic-tangent type, characteristic for shear layers. As mentioned in Section 2, this profile was used to calculate the shear parameter λ from the velocities at points 1 and 2.

The turbulent stresses $-\rho\overline{u'v'}$, $\rho\overline{u'^2}$ and $\rho\overline{v'^2}$ are shown in Figs. 4b-c. The plates are set close to the positions where these quantities are maximum. The mean vertical vorticity (with reversed sign for clarity) $-\overline{\omega_z} = -\partial\overline{v}/dx + \partial\overline{u}/dy$ is shown in Fig. 4d. The vorticity maximum (located at $y/B \approx 0.1$), which also indicates the inflection point of $\overline{u}(y)$, is slightly shifted towards the high-speed side, relative to the maximum of turbulent shear stress (at $y/B \approx -0.1$). Such shifts between maximums of turbulent stresses and maximum of time-averaged vorticity (inflection point) were also observed in plane shear layers (Wygnanski and Fiedler, 1970; Mehta and Westphal, 1986).

3.2. Turbulent stresses

The left column of Fig. 5 shows the turbulent shear stress $-\overline{u'v'}$ for the five flow cases. As slight variations in the incident flow are observed among the flow cases, the turbulent shear stress is normalised by $-\overline{u'v'}_{max,up}$, the maximum of the lateral profile $-\overline{u'v'}(y)$ of the incident flow, this latter profile being spatially averaged in streamwise direction between $(x - x_t)/L_s = -1.08$ and -0.80. The values of $-\overline{u'v'}_{max,up}$ for the five flows are reported in Table 3. In Fig. 5 and in similar figures thereafter, the position of the plates is depicted by solid or dashed black lines, whose solidity is equal to the solidity of the plates. However, the positions of the holes do not correspond to that of the plates and the plate thicknesses are not to scale.

Consider first the solid plate S100, which reduces the turbulent shear stress $-\overline{u'v'}$ the most. Alongside the plate, $-\overline{u'v'}$ is effectively reduced to zero and that almost immediately after the leading edge. A short distance after the trailing edge, regions of weak positive and negative $-\overline{u'v'}$ appear, respectively on the high-speed and on the low-speed side of the plate, characteristic of a wake. About $0.5L_s$ downstream of the trailing edge, the negative $-\overline{u'v'}$ disappears while the positive one starts to progressively increase downstream. At the end of the measurement section, $1.8L_s$ downstream of the plate's trailing edge, the turbulent shear stress did not recover yet its upstream undisturbed value.

For all of the porous plates examined (S17, S33 and S67), the turbulent shear stress is not reduced to zero alongside the plate, contrary to S100. Moreover, the positive $-\overline{u'v'}$ now increases abruptly at the plates' trailing edge, and for S17 and S33, it becomes even higher than the turbulent shear stress of the incident flow. In all three cases, $-\overline{u'v'}$ then decays within a distance of approximately 0.5 to $1.5L_s$, after which $-\overline{u'v'}$ is lower than the value of the incident flow. As for the solid plate S100, a region of negative turbulent shear stress characteristic of wake is observed on the low-speed side, but with much lower intensities as the positive peaks of $-\overline{u'v'}$.

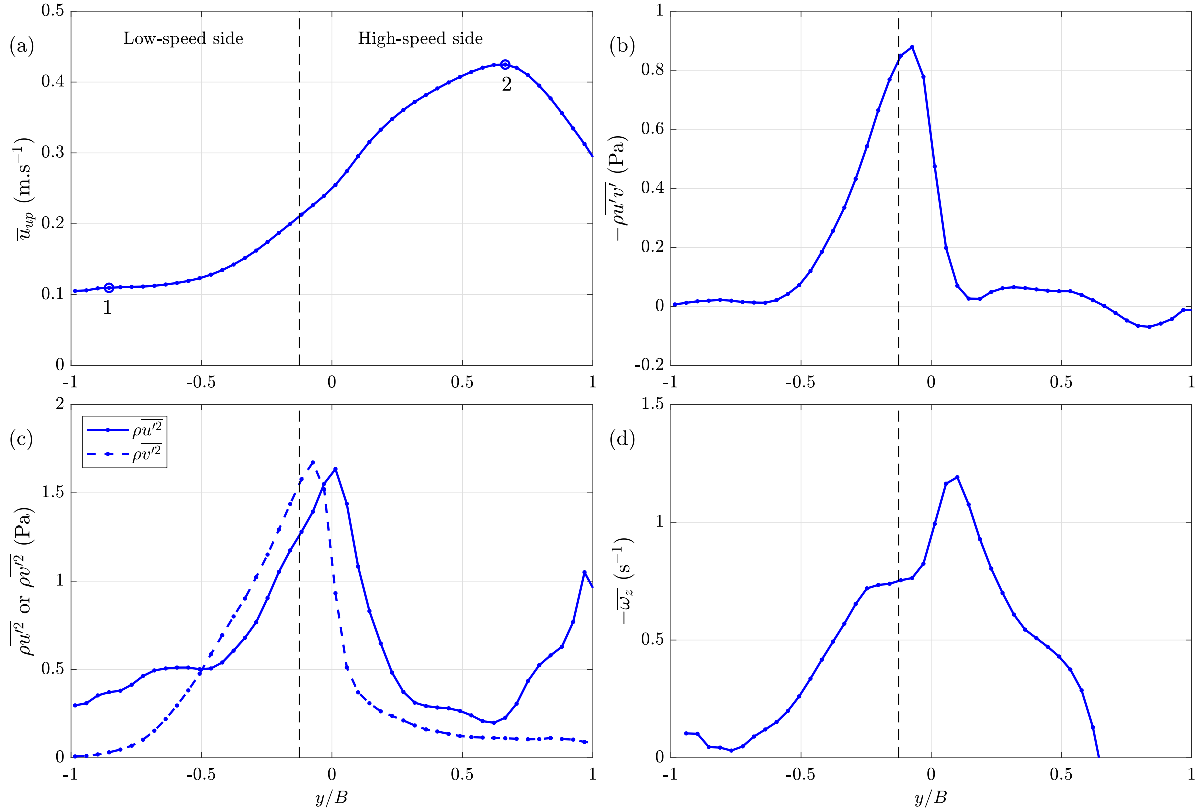

Fig. 4. Lateral profiles spatially averaged between $(x-x_t)/L_s = -1.08$ and -0.80 for the reference flow S0 of (a) $\overline{u}$, (b) $-\rho\overline{u'v'}$, (c) $\rho\overline{u'^2}$ and $\rho\overline{v'^2}$, and (d) $-\overline{\omega_z}$. The position where the plate is installed for the remaining flow cases is indicated by the vertical dotted line. In (a), the points 1 and 2 correspond to the positions where the velocities U_1 and U_2 are taken for calculating the shear parameter λ.

Table 3

Quantities used for normalising the turbulent stresses, the vorticity and Q_v in Figs. 5, 6, 11, 12 and 13. The operator $(\cdot)_{max,up}$ designates the maximum of the lateral profile of the quantity for the incident flow, spatially averaged in the streamwise direction between $(x-x_t)/L_s = -1.08$ and -0.80 (for Figs. 5 and 6). The operator $(\cdot)_{up}$ designates a spatially averaged quantity in the streamwise direction between $(x-x_t)/L_s = -1.08$ and -0.80 (for Figs. 11b and 11c). The operator $\langle\cdot\rangle_{max}$ designates the maximum value in the lateral profile of the quantity obtained by spatially averaging the ensemble-averaged field in streamwise direction between $(x-x_t)/L_s = 0$ and 1 for S0, S17 and S33 and between $(x-x_t)/L_s = 0.25$ and 0.75 for S67 and S100 (for Figs. 12 and 13).

	$-\rho\overline{u'v'}_{max,up}$	$\rho\overline{u'^2}_{max,up}$	$\rho\overline{v'^2}_{max,up}$	$-\overline{\omega}_{z\,max,up}$	$\langle Q_v\rangle_{T,up}$	$-\langle\omega_z\rangle_{T,up}$	$-\rho\langle\overline{u'v'}\rangle_{max}$	$\rho\langle\overline{u'^2}\rangle_{max}$	$\rho\langle\overline{v'^2}\rangle_{max}$
	(Pa)	(Pa)	(Pa)	(s^{-1})	(s^{-2})	(s^{-1})	(Pa)	(Pa)	(Pa)
S0	0.88	1.63	1.67	1.19	0.70	1.81	0.89	1.65	1.80
S17	0.69	1.45	1.47	1.09	0.67	1.78	0.73	2.01	1.44
S33	0.67	1.49	1.34	0.96	0.60	1.70	0.81	2.32	1.08
S67	0.80	1.59	1.35	1.18	0.61	1.78	0.62	2.71	0.63
S100	0.79	1.36	1.62	1.07	0.67	1.77	0.29	1.43	0.41

The right column of Fig. 5 shows the vertical vorticity of the time-averaged flow $-\overline{\omega_z} = -\partial\overline{v}/dx + \partial\overline{u}/dy$, normalised by $-\overline{\omega}_{z\,max,up}$, the maximum of the lateral profile upstream of each plate (see Table 3). As mentioned above, the maximum of the incident vorticity is offset from the plate on the high-speed side. All plates have the effect of increasing the time-averaged vorticity on the high-speed side of the plates. This increase starts roughly at mid-length for all plates. For the porous plates, the region of maximum vorticity is separated from the plates. For the solid plate S100, on the other hand, the vorticity seems to emerge directly from the boundary layer of the plate and the vorticity production is higher than for the porous plates. The vorticity increase is in accordance with the same-sign vorticity associated with the boundary layer on this side of the plates. On the low-speed side of the plates, vorticity cancellation takes place for all plates, which can this time be linked with the opposite-sign vorticity of the boundary layer along this side of the plates. The undisturbed distribution of the vorticity is recovered approximately $1.8L_s$ downstream of the plates' trailing edge, except for S100 for which the overshoot in $-\overline{\omega_z}$ is still noticeable at this position.

The longitudinal turbulent normal stress $\overline{u'^2}$ is shown in the left column of Fig. 6, normalised by the upstream maximum $\overline{u'^2}_{max,up}$ (see Table 3). $\overline{u'^2}$ is not reduced by the plates, even for the solid plate S100. For S100, $\overline{u'^2}$ increases slightly on the high-speed side of the plate, especially alongside the plate surface, while it is reduced on the low-speed side. In the wake of S100, $\overline{u'^2}$ follows the path

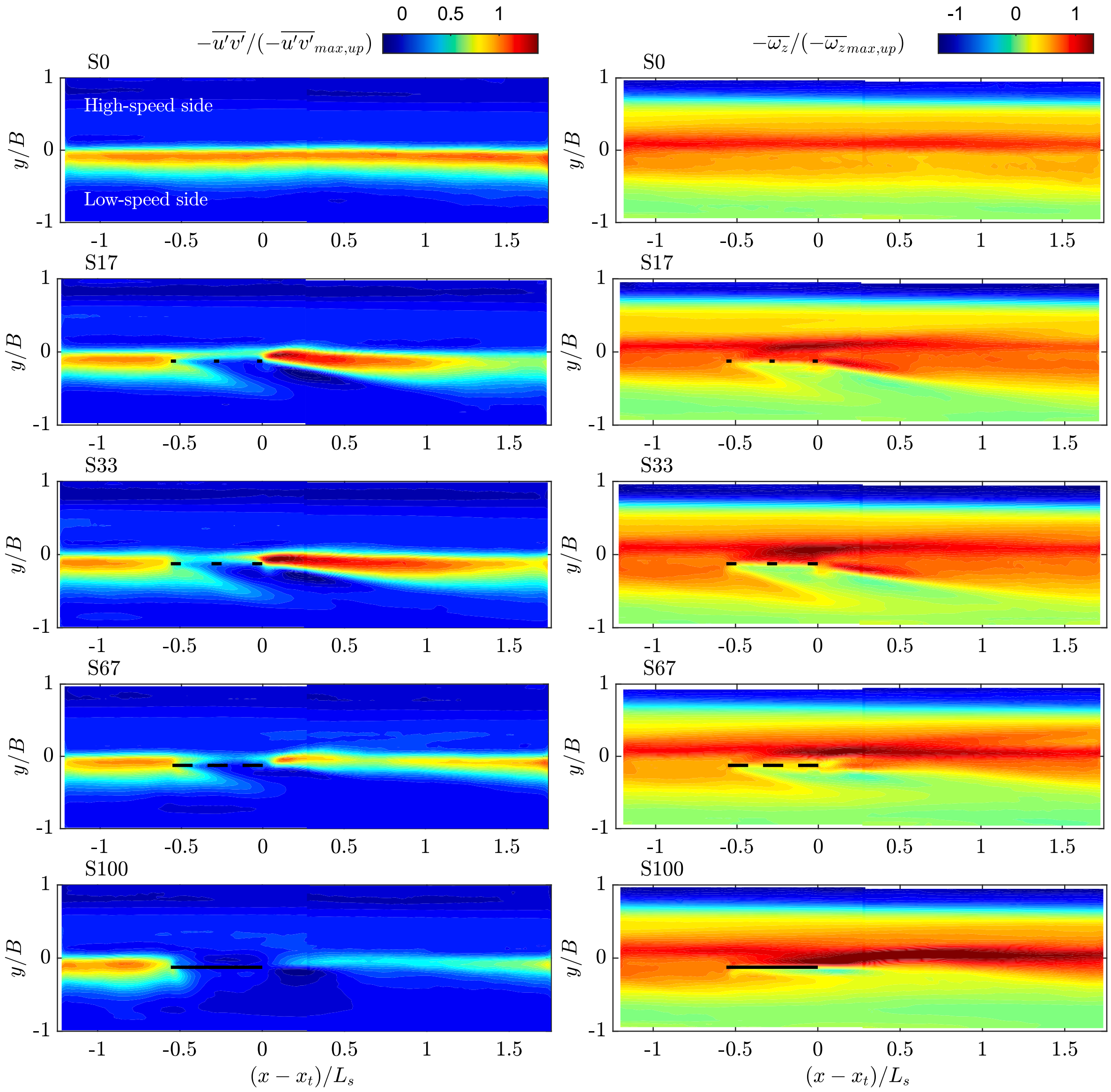

Fig. 5. Left column: turbulent shear stress $-\overline{u'v'}$ for the five flow cases. Right column: time-averaged vertical vorticity $-\overline{\omega_z}$. The quantities are normalised by the maximum value of the lateral profile of the incident flow, spatially averaged between $(x - x_t)/L_s = -1.08$ and -0.80. The plate position is given by the dashed or solid black line (the line solidities are equal to the plate solidities but the holes are not those of the plates). The plate thickness is not to scale.

of the maximum vorticity (right column of Fig. 5) and is slightly higher and more thinly spread than upstream. For the porous plates on the other hand, a strong overshoot in $\overline{u'^2}$ is observed, which starts at about mid-length of the plate, congruent with the increase in time-averaged vorticity. The overshoots all peak near the trailing edge and then decay rapidly downstream. The undisturbed value is recovered at the end of the measurement section ($1.8L_s$ downstream of the plate trailing edge) for S17 and S33 but not yet for S67. While the intensity and length of the overshoot in $\overline{u'^2}$ increase as the solidity of the porous plates increases, the overshoot does not form in the case of the solid plate S100. The evolution of $\overline{u'^2}$ is therefore not monotonic with solidity S. Only the presence of holes in the plate is seen to increase $\overline{u'^2}$.

The right column of Fig. 6 shows the lateral turbulent normal stress $\overline{v'^2}$ normalised by the upstream maximum $\overline{v'^2}_{max,up}$ (see Table 3). All the plates have the effect of drastically reducing the lateral fluctuations alongside the plate and this reduction increases monotonically with plate solidity. For the solid plate S100, the lateral fluctuations are necessarily reduced to zero at the plate surface, but they are also reduced further laterally from the plate on both sides. In the plates' wakes, the same dependency on solidity is observed: weaker $\overline{v'^2}$ with increasing solidity. For all plates, a local increase in $\overline{v'^2}$ is observed downstream of the plate, with some distance from the plate trailing edge, and which for S17 slightly overshoots the upstream value. This local maximum in $\overline{v'^2}$ becomes

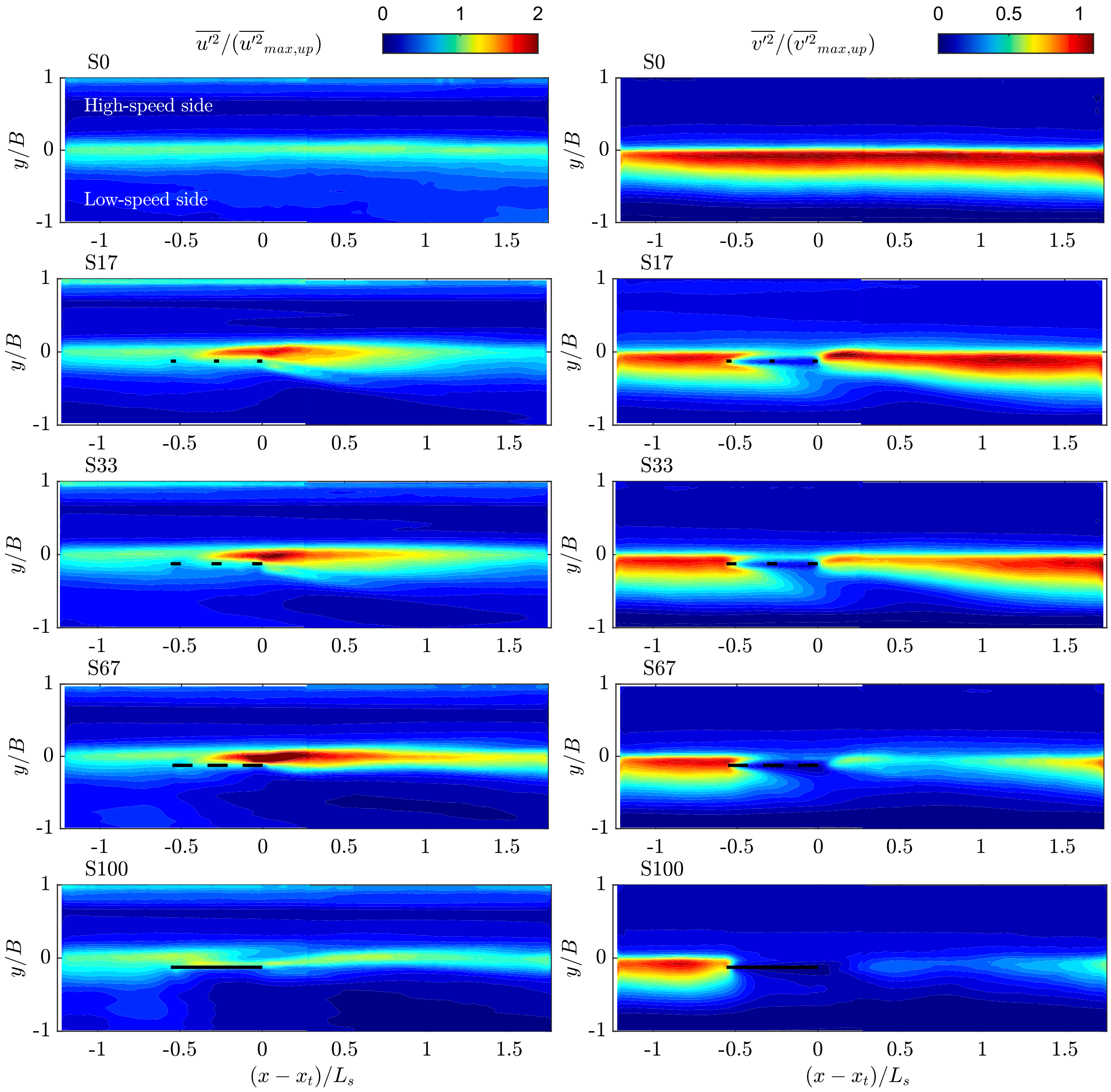

Fig. 6. Left column: longitudinal turbulent normal stress $\overline{u'^2}$ for the five flow cases. Right column: lateral turbulent normal stress $\overline{v'^2}$. The quantities are normalised by the maximum value of the lateral profile of the incident flow, spatially averaged between $(x - x_t)/L_s = -1.08$ and -0.80. The plate position is given by the dashed or solid black line (the line solidities are equal to the plate solidities but the holes are not those of the plates). The plate thickness is not to scale.

weaker with increasing solidity. In summary, the evolution of $\overline{v'^2}$ is monotonic with solidity S for plates S17 to S100, similarly to $\overline{u'v'}$ but contrary to $\overline{u'^2}$, which behaves differently for the solid plate.

3.3. Velocity deficits in the plates' wake

Fig. 7a shows the lateral profiles of the normalised velocity deficit $(\overline{u}(y) - \overline{u}_{up}(y))/U_Q$ at $(x - x_t)/L_s = 0.11$, where $\overline{u}_{up}(y)$ is the lateral profile upstream of each plate spatially averaged between $(x - x_t)/L_s = -1.08$ and -0.80 (for S0, this profile is shown in Fig. 4a). The non-zero value for the reference case S0 indicates variations of the base flow due to the development of the shear layer, which is not completely achieved at the measurement position. It can nevertheless be seen that the velocity deficit in the plate wake increases with plate solidity. For S100, a maximum velocity deficit of about 15% of the bulk velocity U_Q is generated by the plate at this position.

Fig. 7b shows the longitudinal evolution of the velocity deficit in the plate wake for S100. The profile of $(\overline{u}(y) - \overline{u}_{up}(y))/U_Q$ is plotted at different distances $(x - x_t)/L_s$ from the plate trailing edge. Assuming a 1/7-power-law velocity profile for the turbulent

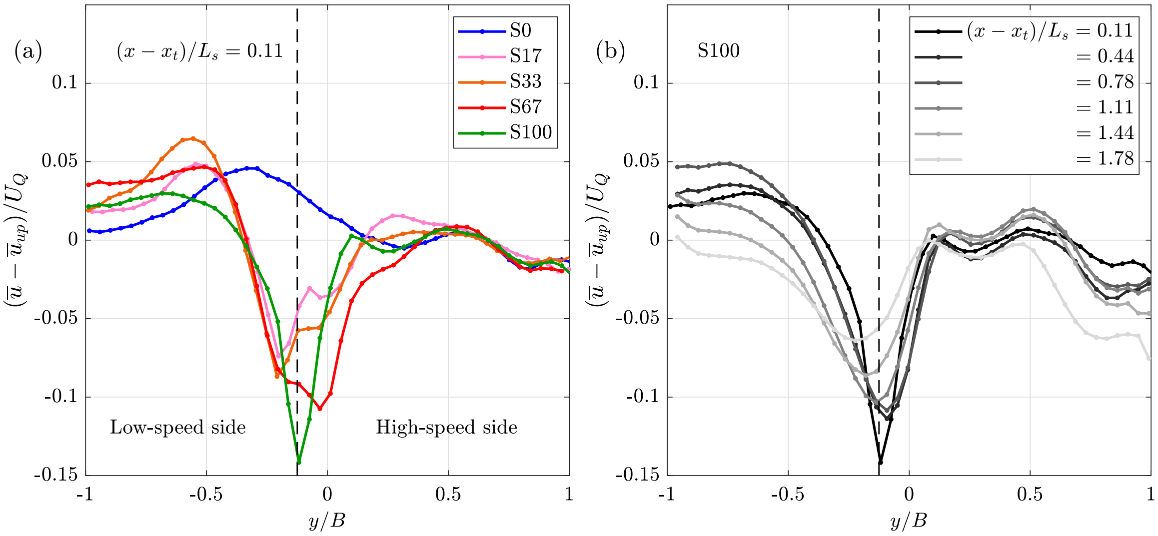

Fig. 7. (a) Lateral profiles of the normalised velocity deficit $(\overline{u}(y) - \overline{u}_{up}(y))/U_Q$ at $(x - x_t)/L_s = 0.11$, where $\overline{u}_{up}(y)$ is the lateral profile upstream of each plate (spatially averaged between $(x - x_t)/L_s = -1.08$ and -0.80). (b) Lateral profiles of the normalised velocity deficit $(\overline{u}(y) - \overline{u}_{up}(y))/U_Q$ for flow case S100 at different streamwise locations $(x - x_t)/L_s$ downstream of the plate trailing edge. The plates' position is indicated by the vertical dotted line.

boundary layer growing on the plate (White, 1991), the boundary layer thickness at the end of the plate (on one side) is about $\delta = 0.16L^{6/7}(\nu/U_0)^{1/7} = 15\,\text{mm} = 0.04B$, where U_0 is the velocity at the y-position of the plate. This thickness is much lower than the width of the velocity deficit for the profile closest to the plate at $(x - x_t)/L_s = 0.11$. The velocity deficit therefore cannot be solely ascribed to the turbulent boundary layer growth on the plate.

As for a typical wake flow, the velocity deficit decreases with streamwise distance and the wake widens. At $1.78L_s$ downstream of the plate trailing edge, the velocity deficit is reduced by one half of its value at $0.11L_s$. Cousteix et al. (1989) found a similar wake behaviour for a LEBU, with a complete decay of the velocity deficit 4δ downstream of the plate trailing edge, with δ the boundary layer height.

3.4. Spatial correlations

The Kelvin–Helmholtz structures induce a specific large-scale spatial correlation of the velocity field, which is also one of the best indicator of their presence (Dupuis et al., 2023b). Investigating how the plates affect the spatial correlation will therefore help to understand how the plates disturb or do not disturb the Kelvin–Helmholtz structures and where the strongest disturbances are localised.

The left column of Fig. 8 shows the two-point spatial correlation of the longitudinal velocity fluctuation

$$R_{uu}(x,y) = \frac{\overline{u'(t,x_0,y_0)u'(t,x,y)}}{\left(\overline{u'^2(t,x_0,y_0)}\;\overline{u'^2(t,x,y)}\right)^{1/2}} \tag{2}$$

for the five flow cases, with the reference point (x_0, y_0) set at $(x_0 - x_t)/L_s = 0.5$ and $y_0/B = -0.06$. In the absence of a plate (case S0), the presence of the Kelvin–Helmholtz structures leads to a periodic pattern of R_{uu} with a periodicity of approximately 0.9 m, which was used to determine the average length of the structures L_s. The correlation pattern is characterised by strong values in the floodplain and by a skewed shape. The plates have the effect of weakening the spatial correlation, although the general pattern and the periodicity are still maintained downstream of the plates. The correlation pattern is altered the most for S100, but is still recognisable. For S100, and to a lesser extend for S67, a structural difference can be observed, however: A region of positive correlation appears on the low-speed side of the plate's trailing edge. This suggests the presence of structures of smaller spatial periodicity (about $0.5L_s$).

The two-point space correlations of the lateral velocity fluctuation, R_{vv}, are shown in the right column of Fig. 8, for the same reference point as for R_{uu}. As for R_{uu}, the pattern of R_{vv} for the undisturbed flow (S0) extends mostly in the floodplain and features a periodicity of about 0.9 m. However, contrary to R_{uu}, the pattern is not skewed but nearly invariant in lateral direction. The pattern of R_{vv} is more weakened by the plates than that of R_{uu}. This is to be expected since the streamwise-oriented plates act stronger on the lateral fluctuations, as they crash against the plates. However, a remnant of the large-scale spatial correlation is still present downstream of each plate. As for R_{uu}, R_{vv} displays for S100 a local positive value on the low-speed side of the trailing edge, corresponding to a periodicity of about $0.5L_s$.

When the reference point (x_0, y_0) is set towards the end of the measurement section at $(x_0 - x_t)/L_s = 1.4$ (not shown, see Dupuis et al., 2025), the correlation patterns of both u' and v' are nearly completely recovered for S17 and S33, while it is partly rebuilt but not completely recovered for S67 and S100.

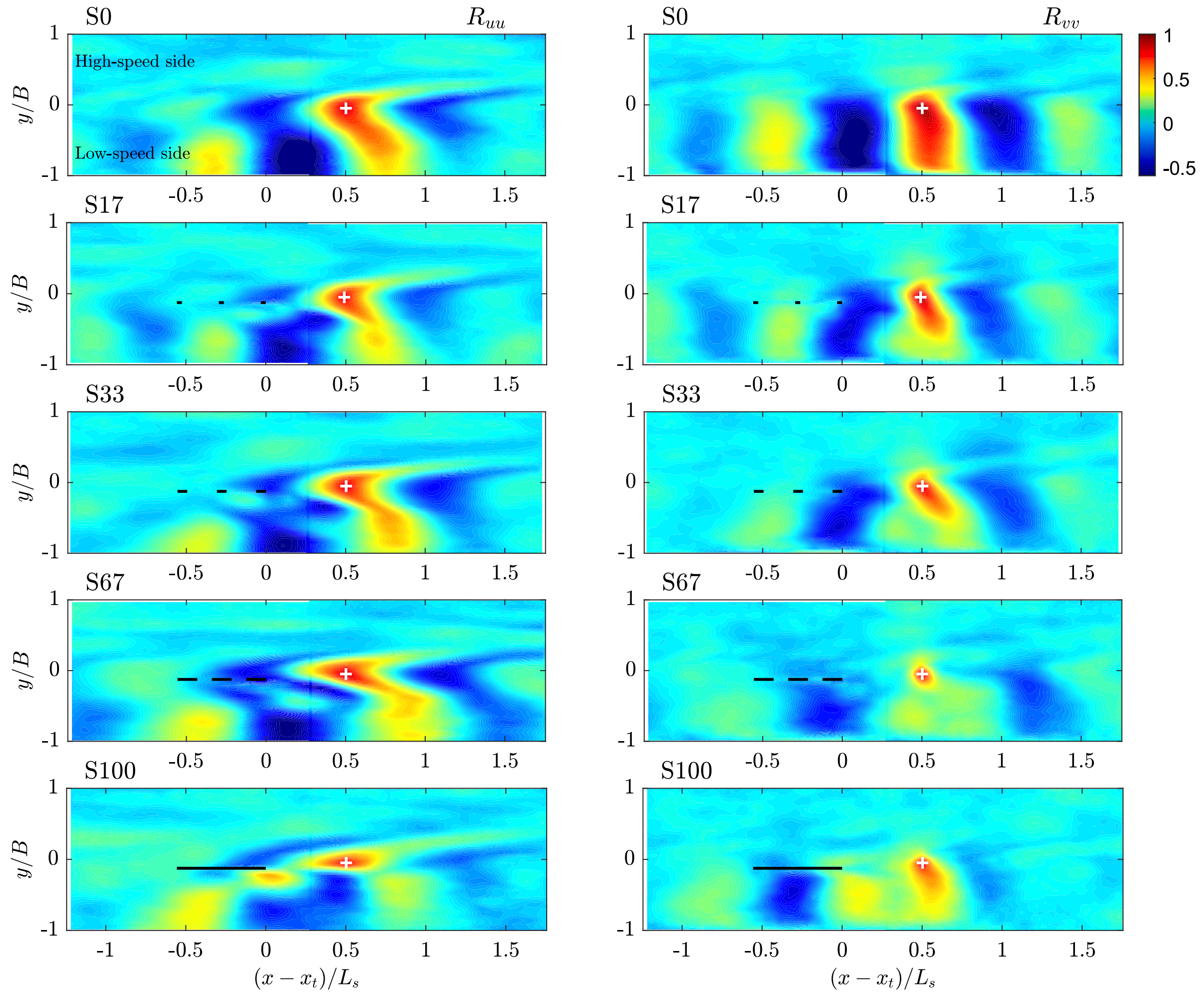

Fig. 8. Two-point space correlation of (left column) the longitudinal velocity fluctuation R_{uu} and (right column) the lateral velocity fluctuation R_{vv} for the five flow cases, with the reference point $(x_0,\ y_0)$ set at $(x_0-x_t)/L_s = 0.5$ and $y_0/B = -0.06$. The reference point is indicated by a white cross. The plate position is given by the dashed or solid black line (the line solidities are equal to the plate solidities but the holes are not those of the plates). The plate thickness is not to scale.

3.5. Tracking of the Kelvin–Helmholtz vortices

The objective of the present section is to investigate the fate of the Kelvin–Helmholtz vortices when passing the plates. To this end, a vortex tracking technique was implemented based on the Q-criteria (Epps, 2017), which in 2D reduces to the determinant of the Jacobian matrix of the 2D velocity vector and which we denote herein Q_v to distinguish from the discharge. Since Q_v consists of spatial derivatives of the velocity, which are highly sensitive to measurement noise, the raw velocity fields were spatially smoothed, using an adaptive Gaussian window as described in Fouras and Soria (1998). The size of the smoothing window was 7 × 7 grid points, corresponding to $12.2 \times 12.2\,\text{cm}^2$ (i.e. a side length of $0.16L_s$).

Fig. 9 shows typical snapshots of the smoothed velocity fields for cases S0 and S100. In this figure, a convection velocity of $U_c = 0.19\,\text{m.s}^{-1}$ was removed from the longitudinal component of the velocity (the convection velocity is discussed later in this Section). The slight discontinuity in the velocity field at $(x-x_t)/L_s = 0.26$ corresponds to the interface between the two cameras. Q_v is plotted in background colour. The Kelvin–Helmholtz vortex street, characterised by a train of same-sign vortices separated by saddle points, dominates the entire span of velocity field for S0, while it is weakened downstream of the plate S100. Local maxima of Q_v correspond well to positions of vortex cores identified in the velocity field.

To start the vortex tracking, local maxima of Q_v at the streamwise position $(x-x_t)/L_s = -1$ above a threshold value of $0.45\,\text{s}^{-2}$ were detected. Then, each of these local maxima was tracked in positive and negative time, using a search box of size $33 \times 33\,\text{cm}^2$ (corresponding to 43% of L_s), in which the maximum of Q_v was identified in the next time step. The position of the detected local maximum of Q_v is noted (x_V, y_V), the index V standing for vortex core. If the maximum of Q_v went below a threshold of $0.06\,\text{s}^{-2}$,

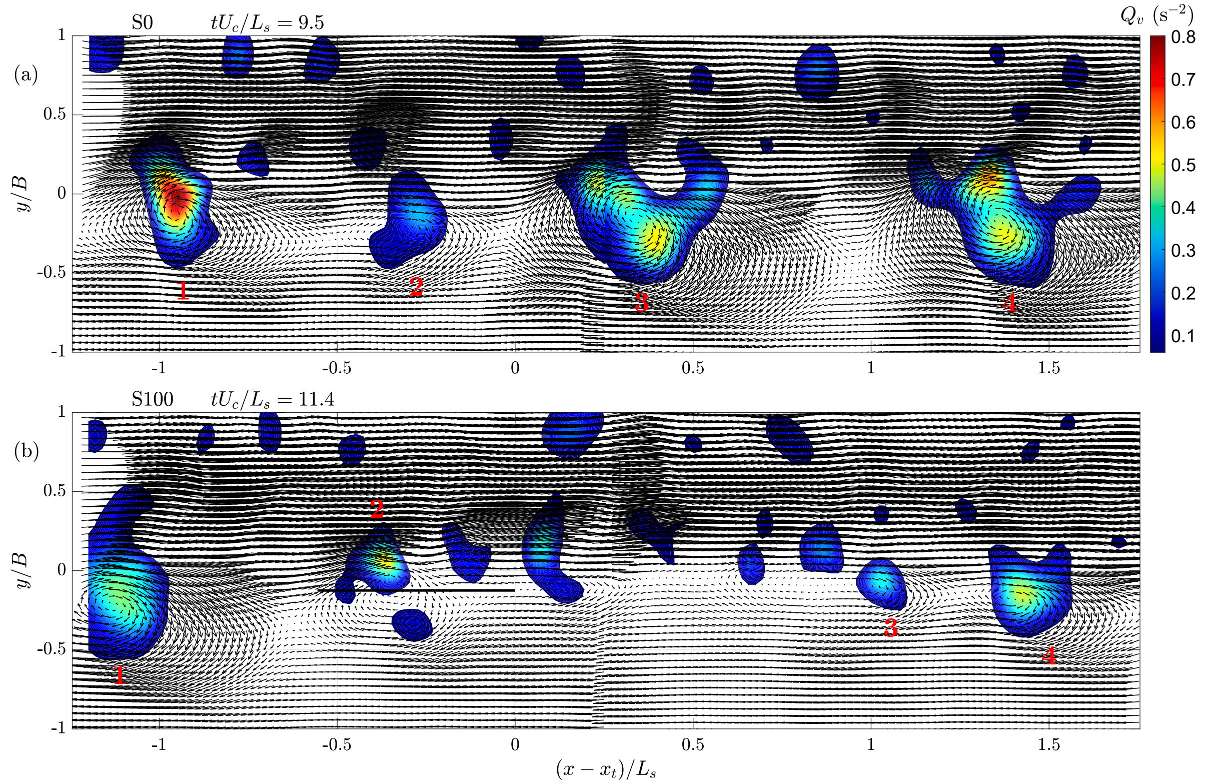

Fig. 9. Instantaneous velocity field $(u - U_c,\ v)$ for (a) case S0 at $tU_c/L_s = 9.5$ and (b) case S100 at $tU_c/L_s = 11.4$. The background colour is Q_v with the threshold $Q_v > 0.06\,\mathrm{s}^{-2}$. In (b), the plate position is indicated by a black line.

the tracking was stopped (below this threshold, also used in Fig. 9, the vortex core can be considered as disintegrated). Tracked vortices are identified in Fig. 9 with numbers (discussed further below).

For each flow case, around 40 vortex trajectories were detected and no trajectory was aborted before the end of the measurement section (i.e. the local maximum of Q_v never went below the threshold $0.06\,\mathrm{s}^{-2}$). This implies that for each flow case, all vortices detected at $(x - x_t)/L_s = -1$ passed the plate without having their core destroyed. This is in accordance with the persistence of the spatial periodicity observed in the correlation pattern as the flow passes the plates (see Section 3.4).

Figs. 10a-b show the streamwise position of the detected vortex cores as a function of time, $x_V(t)$, for the reference case S0 and for the solid plate S100 respectively. Blue and red colours are used to distinguish more easily successively occurring trajectories. Some vortex mergers are observed, marked with black circles. These mergers correspond to vortices that weaken and that are progressively absorbed by a neighbouring vortex (usually by the upstream vortex). The slope of $x_V(t)$ gives the convection velocity of the vortex cores. The undisturbed convection velocity of the cores has a mean value of $U_c = 19\,\mathrm{cm.s}^{-1}$ and was used to plot the vector fields in Fig. 9. This velocity is 25% smaller than the local time-averaged velocity at the mean position of the vortex cores (i.e. $y/B = -0.025$, see Fig. 11a discussed below). For case S100 (Fig. 10b), an increase in the slope of $x_V(t)$ is observed at the level of the plate (grey area), corresponding to an increase in the convection velocity of the vortex cores of 50%. At a distance L_s downstream of the plate trailing edge, the convection velocity then recovers its undisturbed value.

The vertical dashed lines in Figs. 10a and 10b indicate the time at which the instantaneous velocity fields in Fig. 9 are plotted, for S0 and S100 respectively. For S0 at $tU_c/L_s = 9.5$ (Fig. 9a), four vortices are present in the measurement section. Vortex 2 is weaker than the others but its core is still recognisable as well as the two flanking saddle points. For vortices 3 and 4, there are multiple local Q_v-maxima within the same vortex (only the strongest of which is detected for the vortex tracking), a feature which is very often observed. This probably corresponds to formerly separated vortex cores which are not completely merged. For S100 at $tU_c/L_s = 11.4$ (Fig. 9b), four vortices are also detected. Other local Q_v-maxima are present in the floodplain edge region, but inspection shows that they rapidly disappear or are absorbed by neighbouring vortices, a phenomenon comparable to the tearing process described by Bernal and Roshko (1986).

In order to determine the average characteristics of the vortex cores passing the plates, different flow quantities were phase-averaged with respect to the detected trajectories for a given x-position (in other words, an average is carried out at a given x-position over all detected trajectories). Quantities averaged in this manner are denoted by $\langle\cdot\rangle_T$, where the index T stands for trajectories. Fig. 11a shows the mean path of the vortex cores $\langle y_V\rangle_T(x)$ with 95% confidence intervals for all five flow cases. Although the measurement scatter is quite high due to the limited number of samples, it can be seen that, compared to the reference case S0, the

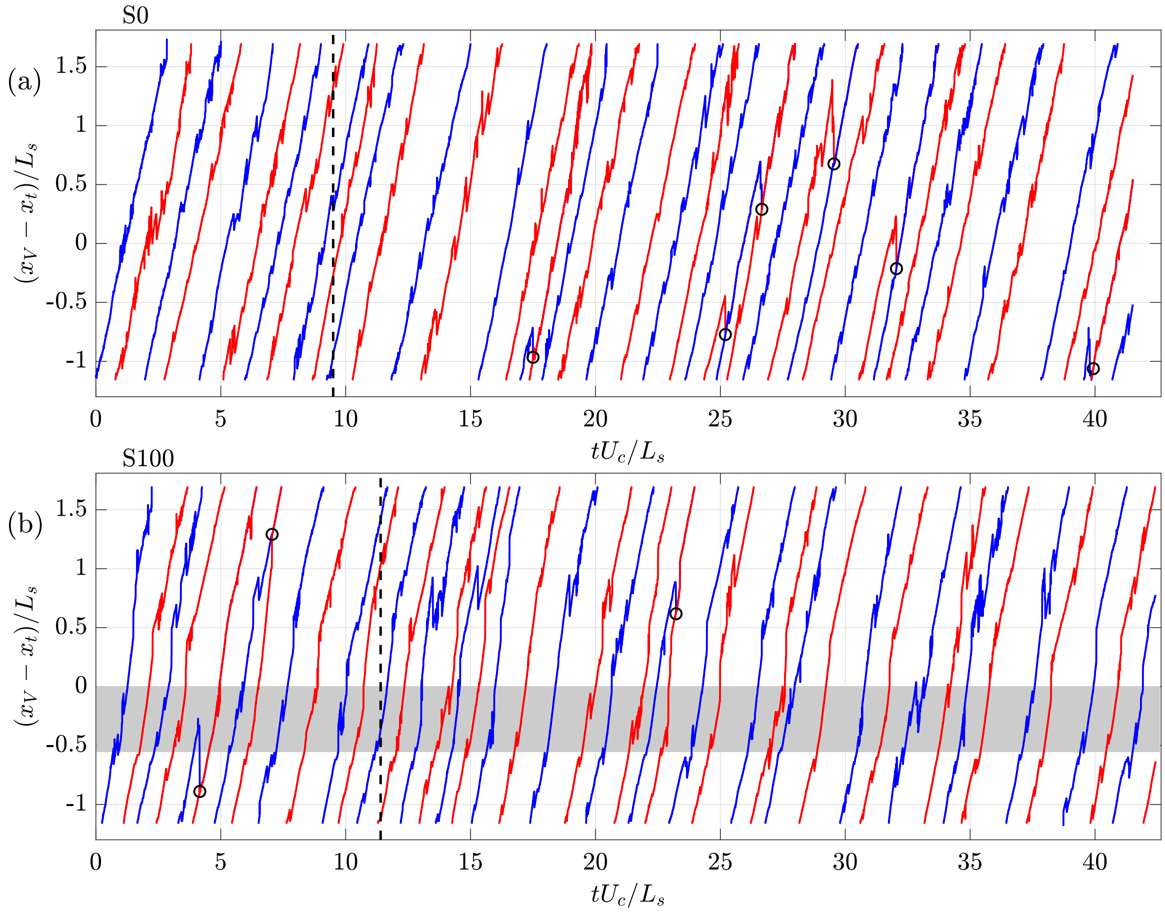

Fig. 10. (a) Temporal variation of the streamwise position of the detected vortex cores $x_V(t)$ for (a) case S0 and (b) case S100. Black circles indicate position of vortex mergers. The vertical dashed line in each plot indicates the time at which the instantaneous velocity fields of Fig. 10 are plotted. The grey strip in (b) indicates the position of the plate.

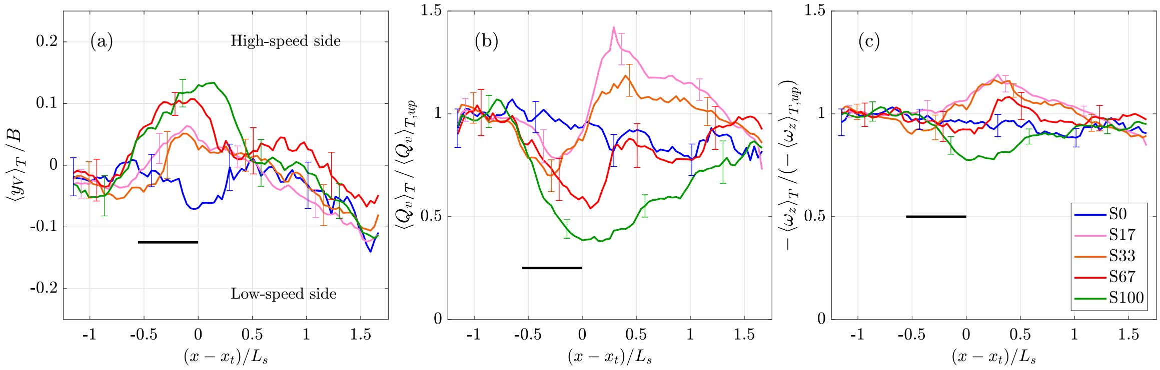

Fig. 11. (a) Mean trajectory of the vortex cores (averaged over all detected trajectories for each flow case). (b) Mean Q_v-value of the vortex cores along the trajectories, normalised by the value of the incident flow $\langle Q_v \rangle_{T,up}$. (c) Mean vertical vorticity of the vortex cores along the trajectories, normalised by the value of the incident flow $\langle \omega_z \rangle_{T,up}$. The error-bars represent 95% confidence intervals. The black horizontal line represents the streamwise position of the plates (in (a) also the lateral position).

plates have the tendency to shift the vortex cores towards the high-speed side. This shift is higher when the solidity of the plate increases. The maximum deviation, obtained for S100, is on the order of $0.15B$ to the high-speed side. Downstream of the plates, the vortices move back towards the low-speed side and at about $(x - x_t)/L_s = 1$ they recover their undisturbed position.

The increase in convection velocity of the vortex cores observed for S100 in Fig. 10b can be explained by the shift exerted by the plate on the vortex cores towards a region of higher velocity. A similar increase in convection velocity alongside the plate was observed for S67 (not shown), while no significant increase was detected for S17 and S33, in accordance with the smaller lateral shift of the vortex cores for these cases.

Fig. 11b shows the mean Q_v-value of the vortices, $\langle Q_v \rangle_T$, normalised by the value of the incident flow for each case, $\langle Q_v \rangle_{T,up}$ (see Table 3). For all plates, a decrease in $\langle Q_v \rangle_T$ is first observed, which begins slightly upstream of the plates at $(x - x_t)/L_s \approx -0.7$ and which becomes more pronounced with increasing plate solidity. For S100, the decrease in $\langle Q_v \rangle_T$ continues till the plate trailing edge, where it reaches $-60\,\%$ of the undisturbed value. $\langle Q_v \rangle_T$ then increases progressively, until it recovers the reference case value at $(x - x_t)/L_s \approx 1.5$. For the porous plates S17 and S33, a strong increase in $\langle Q_v \rangle_T$ starts at around half-length of the plate, ending with an overshoot of Q_v, which reaches +40% of the undisturbed value for S17. S67 also features a sudden increase in $\langle Q_v \rangle_T$ but only at the trailing edge of the plate and without exceeding the undisturbed value. As for the solid plate S100, for all porous plates the undisturbed value is reached about $1.5L_s$ downstream of the plate trailing edge.

Fig. 11c shows the mean vertical vorticity ω_z at the position of the detected vortex cores, $\langle \omega_z \rangle_T$, normalised by the value of the incident flow $\langle \omega_z \rangle_{T,up}$ (see Table 3). The tendency is almost the same as for $\langle Q_v \rangle_T$, except that no decrease in $\langle \omega_z \rangle_T$ is observed for the porous plates when encountering the plate. In addition, the relative variations are smaller: The maximal decrease in $\langle \omega_z \rangle$ for S100 is −20% and the maximal overshoot for S17L +20% of the undisturbed value. An overshoot in $\langle \omega_z \rangle_T$ is observed for all porous plates. As for $\langle Q_v \rangle_T$, the vortex cores recover their undisturbed vorticity about $1.5L_s$ downstream of the plate trailing edge for all plates.

The reason for the overshoot in Q_v and $\langle \omega_z \rangle_T$ for the porous plates could be due to vorticity shed through the holes of the plates, which feeds the Kelvin–Helmholtz vortex cores. It was indeed observed in Fig. 5 (right column) that the time-averaged vorticity increases in this region on the high-speed side of the porous plates, where the vortex cores pass, in agreement with the sign of the boundary layer vorticity alongside the plates.

The plate S100 is thus the only one that induces a weakening of the incident vortices, in terms of the vorticity of their cores. However, this plate is not long enough to weaken the vortex cores till disaggregation. The porous plates have the opposite effect of rather reinforcing the vortex cores.

3.6. Ensemble-averaged Kelvin–Helmholtz vortices in the plates' near wake

The aim of the present section is to evaluate the contribution of the Kelvin–Helmholtz structures to the changes in turbulence introduced by the plates, observed in Section 3.2.

The detection of the vortex cores in Section 3.5 was used to perform an ensemble-average of the vortices downstream of the plates in order to educe the mean shape of the Kelvin–Helmholtz structures in the near wake. For each flow case, the velocity fields around the vortex cores detected at the position $(x - x_t)/L_s = 0.5$ were averaged among all the detected vortex cores, over a window of length $1.15L_s$ and of width $1.56B$. The ensemble-averaging was done with the raw velocity field and not with the smoothed one. The ensemble-averaged velocity field obtained in this way is noted (u_{EA}, v_{EA}) and is plotted in the left column of Fig. 12 for each flow case, after subtraction of a convection velocity $U_c = 0.19\,\mathrm{cm.s^{-1}}$ (determined above from Fig. 10). The ensemble-averaged velocity field is positioned in space such that the centre is at $(x - x_t)/L_s = 0.5$ and laterally at the mean position of the vortex cores. For all cases a vortex is clearly identified in the centre of the ensemble-averaged velocity field. For S0, S17 and S33 the ensemble-averaged velocity field is periodic, a clear saddle point is located upstream of the vortex centre and the ensemble {vortex + saddle point} occupies the full structure length L_s. For S67 and S100 however, the vortex appears smaller and no saddle points can be observed. For the latter two cases, the velocity field rapidly becomes streamwisely-invariant or 'washed out' away from the vortex core, such that the educed structure occupies only part of the length L_s.

The right column of Fig. 12 shows for each flow case the instantaneous velocity field of a detection, chosen to be representative (again, a convection velocity of $U_c = 0.19\,\mathrm{cm.s^{-1}}$ is subtracted). For S0, a clean Kelvin–Helmholtz roller with its two flanked saddle points is observed. For S17 and S33, the vortices are somewhat smaller and less regular but still close to the case S0. For S67 however, the vortex in the centre of the ensemble-averaged field is much smaller than for S0 and is flanked by other vortices of same sign and of approximately the same size. The position of these secondary vortices varies considerably from one detection to the other, inducing a dispersion among the detected velocity fields, which explains the washing out of the ensemble-averaged field when going away from the centre, observed on the left column of Fig. 12. For S100 the central vortex is even smaller and weaker. The same phenomenon of secondary vortices as for S67 is observed, but the secondary vortices are also smaller and less intense.

The secondary vortices which accompany the vortex core for S67 and S100 must originate from an interaction between the incident Kelvin–Helmholtz vortex and the plate. An imprint of such an interaction could be seen on the spatial correlation of Fig. 8, where a local maximum of correlation occurs around the plate trailing edge, suggesting vortex formation at the plate level which is correlated with the passage of the Kelvin–Helmholtz structures. Swirydczuk et al. (1993) identified a formation of secondary vortices when a vortex impinges upon a LEBU, but these secondary vortices, which formed on the upper face of the LEBU and which were then shed downstream, were of opposite sign of the incident vortex, while in the present case the secondary vortices are of same sign. Observation of the velocity fields shows that downstream of plates S67 and S100, the secondary cores progressively merge with the main core or disappear through tearing, such that a single core tends to form again.

In order to assess the contribution to turbulence of the Kelvin–Helmholtz structure educed by the ensemble-averaging procedure, a spatial averaging of the ensemble-averaged velocity field was carried out. The spatial averaging operator over the ensemble-averaged field is denoted by $\langle \cdot \rangle_{EA}$ and consists in averaging along a streamwise line centred at the centre of the ensemble-averaged

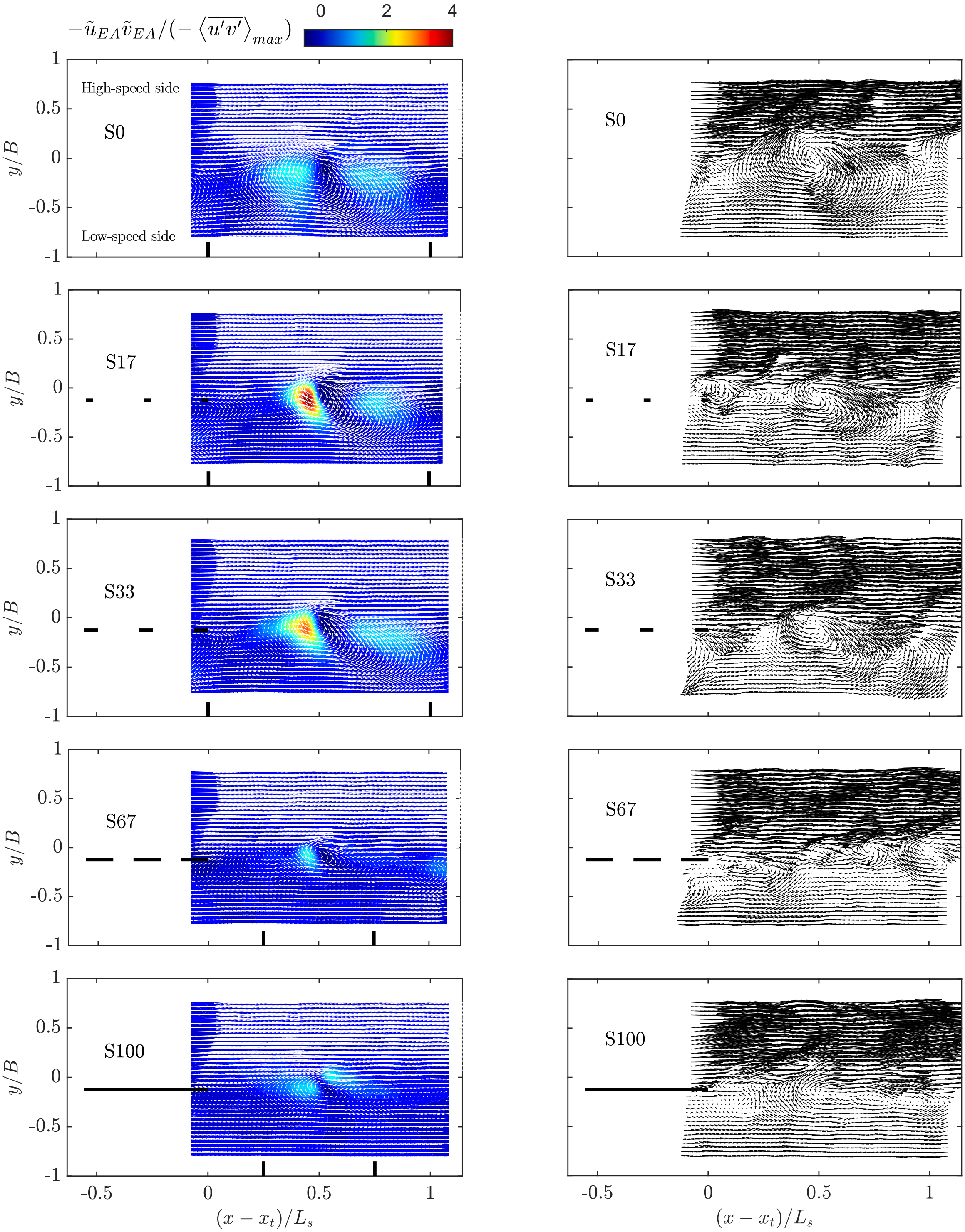

Fig. 12. (left column) Ensemble-averaged velocity field ($u_{EA} - U_c$, v_{EA}) centred at $(x - x_t)/L_s = 0.5$. The two dashes in the bottom of each panel depict the domain over which the spatial averaging is carried out for the quantities in Fig. 13. (right column) Instances of a detected instantaneous flow field used for the ensemble-average. The velocity scale for the vectors (arrows) is the same in all ten panels.

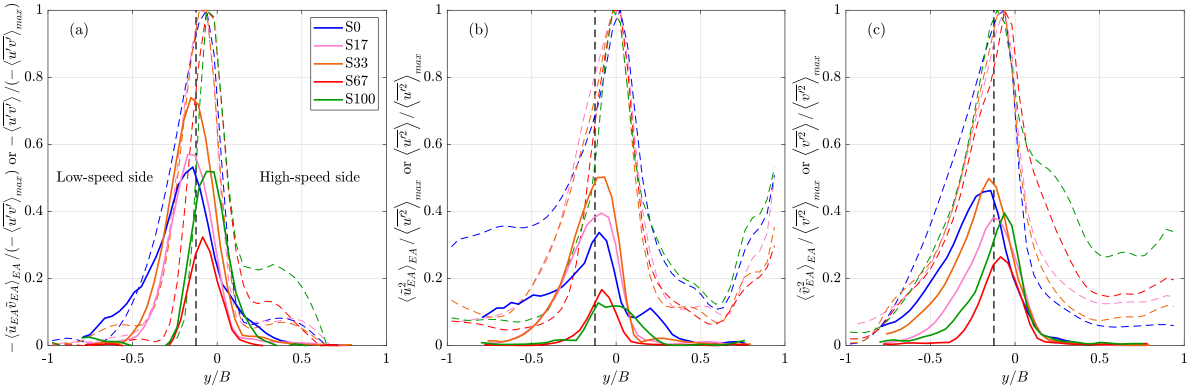

Fig. 13. The solid lines are (a) the turbulent shear stress $-\langle \tilde{u}_{EA}\tilde{v}_{EA}\rangle_{EA}$, (b) the longitudinal turbulent normal stress $\langle \tilde{u}^2_{EA}\rangle_{EA}$ and (c) the lateral turbulent normal stress $\langle \tilde{v}^2_{EA}\rangle_{EA}$ obtained by spatially averaging the ensemble-averaged field over a streamwise length of L_s for S0, S17 and S33 and of $0.5L_s$ for S67 and S100. The dotted lines are the respective quantities of the original flows, spatially averaged over a line of same length and centred at $(x-x_t)/L_s = 0.5$: (a) $-\langle\overline{u'v'}\rangle$, (b) $\langle\overline{u'^2}\rangle$ and (c) $\langle\overline{v'^2}\rangle$. All profiles are normalised by the maximum of the latter profiles. The plates' position is indicated by the vertical black dotted line.

field at $(x-x_t)/L_s = 0.5$. For S0, S17 and S33, the length of this line was chosen to be L_s, while for S67 and S100, since the size of the structures is approximately halved compared to the other cases, the length of the averaging line was set to $0.5L_s$, also corresponding to the local spatial periodicity observed in the near wake of these two plates in the spatial correlation of u (left column of Fig. 8). This choice implies implicitly that for S67 and S100 the plates cut the incident vortex of size L_s into two identical vortices of size $0.5L_s$ (one of them being the main vortex and the other one a secondary vortex). As this choice is somewhat arbitrary, the results have to be considered only qualitatively. The domain over which the spatial averaging is carried out is depicted by the two dashes in the bottom of each panel in the left column of Fig. 12. The spatial fluctuation is denoted by $\tilde{u}_{EA} = u_{EA} - \langle u_{EA}\rangle_{EA}$ and similarly for $\tilde{v}_{EA}$.

The quantity $-\langle \tilde{u}_{EA}\tilde{v}_{EA}\rangle_{EA}$ then represents the turbulent shear stress that is produced by the passing of the educed Kelvin–Helmholtz structure, and represents in this way the contribution of the educed structure to the overall turbulent shear stress $-\overline{u'v'}$. Fig. 13a shows this quantity $-\langle \tilde{u}_{EA}\tilde{v}_{EA}\rangle_{EA}$ (solid lines) for the five flows, together with the lateral profile of the turbulent shear stress $-\langle\overline{u'v'}\rangle$ at $(x-x_t)/L_s = 0.5$ (dashed thin lines), spatially averaged over a streamwise distance of L_s for S0, S17 and S33 and of $0.5L_s$ for S67 and S100. Both quantities are normalised by $-\langle\overline{u'v'}\rangle_{max}$, the maximum value of $-\langle\overline{u'v'}\rangle$, which is reported in Table 3. The same procedure was carried out for the longitudinal and the lateral turbulent normal stress $\langle \tilde{u}^2_{EA}\rangle_{EA}$ and $\langle \tilde{v}^2_{EA}\rangle_{EA}$, shown in Figs. 13b and 13c respectively, together with the spatially averaged profiles at $(x-x_t)/L_s = 0.5$, $\langle\overline{u'^2}\rangle$ and $\langle\overline{v'^2}\rangle$.

For the reference flow S0, the contribution of the educed structure to the turbulent shear stress and to the lateral turbulent normal stress is about 50%, whereas the contribution to the longitudinal turbulent normal stress is about 35%. These values are very close to what we observed in Dupuis et al. (2023a), in which we educed Kelvin–Helmholtz structures based on a Pattern Recognition Technique and followed a similar procedure as described here to assess their contribution to turbulence. The background colour-plot in the left column of Fig. 12 corresponds to the quantity $-\tilde{u}_{EA}\tilde{v}_{EA}$, which indicates which parts of the vortex contribute mainly to the shear stress. As is already known (Ghisalberti and Nepf, 2006), it is the ejection and the sweep located upstream and downstream, respectively, of the vortex core, which contribute the most to the shear stress. The same holds for the longitudinal and lateral normal turbulent stresses (not shown).

For S17 and S33, the contribution of the educed structure to the turbulent stresses is similar or even higher than for the reference flow S0 (Fig. 13), indicating that the changes occurring in the shape of the Kelvin–Helmholtz structure are predominantly responsible for the changes in turbulent stresses observed in Section 3.2. Looking to the left column of Fig. 12, it appears that these changes, as compared to the reference case S0, mainly consist in the strengthening of the ejection located upstream of the vortex core. This strengthened ejection can therefore explain the overshoot in $\overline{u'^2}$ and $-\overline{u'v'}$ observed for these two plates in Section 3.2.

In contrast, for S67 and S100 the contribution of the educed structure to the turbulent stresses is less than for the reference case S0, especially for the lateral fluctuations (Fig. 13b). Furthermore, for these two cases, there is no strengthening of the upstream ejection, as for S17 and S33 (left column of Fig. 12). A possible explanation for this weaker contribution of the educed structure is the presence of the secondary vortices, which contribution may not be reliably assessed with the procedure used (namely by halving the domain of spatial averaging). Alternatively, other flow structures may be present, decorrelated with the Kelvin–Helmholtz vortices and therefore not visible in the ensemble-averaged fields, but which contribute to the turbulent stresses.

4. Comparison with LEBUs

The following discussion aims at comparing the solid plate S100 with the solid LEBU plates. The desired effect of LEBUs is to reduce wall friction by altering the turbulent structures with solid plates oriented parallel to the wall. While the configuration of LEBUs and of the currently investigated plates are different, in both cases the incident turbulence is reduced.

Different mechanisms were put forward to explain how LEBUs reduce the turbulence at the wall and in this way the wall friction. The original idea (Yajnik and Acharya, 1977), which also gave the name to this device (Large-Eddy Break-Up), was that LEBUs destroy the large-scale structures of the boundary layer. Although this explanation was later called into question (Savill and Mumford, 1988), Swirydczuk et al. (1993) pursued this idea, experimentally showing how incident vortices (induced by a pitching mechanism) are weakened by a streamwise-oriented plate. The present investigation tends to confirm that the main effect of the plate is to act on the incident large-scale structures, which are substantially weakened, even if not completely destroyed in the present case.

In an analytical study modelling a line vortex passing above a LEBU under inviscid conditions, Dowling (1985) showed that the plate generates in its wake vorticity first of same sign and then of opposite sign to that of the incident vortex. The opposite sign vorticity is shed at the moment when the incident vortex is in the rear of the plate, such that vorticity cancellation is expected in the wake of the LEBU. Dowling (1985) suggests that the turbulence reduction due to the LEBU is based on this vorticity annihilation. Yet, for the present study, vorticity cancellation can be excluded for explaining the turbulence reduction by the solid plate S100. Indeed, vorticity is globally increased rather than decreased downstream of plate S100 (right column of Fig. 5). The vortex cores lose vorticity, but only alongside the plate, while they regain vorticity downstream of the plate trailing edge (Fig. 11c). Vorticity cancellation takes place, but only over a limited region on the low-speed side of the plate.

For Savill and Mumford (1988) in turn, the main effect of the LEBU is not to destroy existent structures but to introduce new structures into the flow. They showed how the incoming hairpin vortices, which are first cut by the plate, interact with the von Karman vortex street in the plate wake to form new structures which decay downstream. The introduction of new structures was also observed for plate S100, in form of the secondary vortices mentioned in Section 3.6. However, these secondary vortices seem more a result of the turbulence reduction – as pieces of the incident vortex cut by the plate – than the cause of it.

For S100 the turbulent stresses did not recover their undisturbed value at the end of the measurement field, such that the recovery length of the turbulence cannot be assessed precisely. However, by comparing with the porous plates, it seems that the recovery length will not exceed 4 to $5L_s$. Moreover, the statistics of the vortex cores already recovered their undisturbed values $1.5L_s$ downstream of the plate trailing edge (Fig. 11). These recovery lengths seem very low compared to the 100δ recovery length for LEBUs (Savill and Mumford, 1988; Iuso and Onorato, 1995), where δ is the boundary layer thickness. However, both Savill and Mumford (1988) and Iuso and Onorato (1995) showed that the logarithmic law is re-established already 16δ downstream of the LEBU, suggesting that the overall turbulent structure of the boundary layer recovers much faster than the statistics of the undisturbed flow. Also the decay of the velocity deficit in the wake of plate S100 was found similar to what was observed with LEBUs (Section 3.3).

For LEBUs, overshoots in the turbulent stresses are observed locally in the plate wake (Cousteix et al., 1989; Iuso and Onorato, 1995). These overshoots can be ascribed to the wake turbulence of the plate, which is higher than the incoming boundary layer turbulence. This is not the case for S100, as the wake turbulence of the plate is much less intense than the incident shear layer turbulence, such that no turbulence overshoot is observed.

5. Conclusion

The impingement of a turbulent shear layer upon streamwise-oriented plates of different solidities were investigated by means of a large-scale PIV set-up. The shear layer is induced by the velocity difference across the compound cross-section of the channel and contains large-scale Kelvin–Helmholtz structures of mean size $L_s = 0.9\,\mathrm{m}$. The plates' length is $0.56L_s$ and their solidity varies from 17% to 100%. Since the compound channel geometry is maintained downstream of the plates, the undisturbed shear layer reconstitutes progressively downstream of the plates.

The solid plate S100 destroys nearly completely the incoming turbulent shear stress of the shear layer. The remaining shear stress downstream of plate S100 is antisymmetric with respect to the plate and can be ascribed to the plate's wake. For the porous plates, the turbulent shear stress is either not changed (for S67) or increased (for S17 and S33) in the plate near wake. None of the plates induces a decrease in the longitudinal turbulent normal stress in their wake: It is kept constant for S100 but strongly overshoots the undisturbed value for the porous plates. In turn, the lateral turbulent normal stress is decreased for all the plates and this decrease becomes more effective with increasing plate solidity, in accordance with the expected fact that lateral turbulent motions crash against the plates.

For all plates, the incoming Kelvin–Helmholtz structures maintain their integrity when passing the plates, in the sense that their vortex cores, whose paths were determined by a tracking technique, are preserved. In addition, the large-scale spatial correlation of the velocity that characterises the Kelvin–Helmholtz structures is also maintained downstream of the plates, even if importantly weakened for the two most solid plates S67 and S100. The Kelvin–Helmholtz structures therefore appear to be rather robust to perturbations.

The plates induce a slight lateral shift of the vortex cores towards the high-speed side of the shear layer, which induces a local increase in the vortex convection velocity. Downstream of the plates, the vortex cores recover their undisturbed lateral position and convection velocity within a length of L_s.

For the solid plate S100, the vortex cores weaken alongside the plate, in losing continuously vorticity until the plate trailing edge. From the trailing edge onwards, the vortex cores regain progressively vorticity and the undisturbed vorticity is reached $1.5L_s$ downstream of the plate trailing edge. For the porous plates, the response of the vortex cores to the presence of the plate is radically different, as their vorticity is increased, overshooting the undisturbed vorticity. This vorticity strengthening increases when the plates become less solid. A possible explanation for this vorticity increase in the case of the porous plates is same-sign vorticity shed from the holes of the plates and which is absorbed by the vortex cores.

An ensemble-average of the velocity field around the detected vortex cores downstream of the plates enabled to educe the typical shape of the Kelvin–Helmholtz structures in that region. It reveals that the changes in turbulent stresses can be explained for a large part by a change in the shape of the Kelvin–Helmholtz structures. For the plates S17 and S33, the overshoot in turbulent shear stress and in longitudinal turbulent normal stress are due to a more intense ejection upstream of the vortex core, when compared to the undisturbed structure. In turn, the plates S67 and S100 induce a shrinking and weakening of the Kelvin–Helmholtz vortex, but the latter is accompanied by new vortices. These secondary vortices arise from an interaction between incoming structures and plate, which could be roughly described as a cutting of the incoming structure into several pieces. However, further investigations are needed to better characterise this mechanism. The secondary vortices merge progressively downstream with the main vortex core to form a unique core again. For both cases S67 and S100, the contribution of the educed structure to the turbulent stresses is less than for the undisturbed structure, suggesting the presence of other contributing structures, which could be either the secondary vortices or other flow structures not correlated with the Kelvin–Helmholtz structures.

For none of the plates all the turbulent stresses recover completely their undisturbed value at the end of the measurement field, which extends $1.8L_s$ downstream of the plate trailing edge. The recovery length of the turbulence could therefore not be assessed precisely, but it can be concluded that it increases with plate solidity and probably does not exceed 4 to $5L_s$. However, the statistics of the vortex cores were seen to recover their undisturbed values already $1.5L_s$ downstream of the plate trailing edge.

In the present study, the influence of the plate length was not investigated and was determined to correspond to a E-number of 0.12. A solid plate length with this E-value appeared sufficient to destroy locally the incoming turbulent shear stress of a shear layer. Yet, it is not enough to destroy the incident large-scale vortices and the question arises as to which length is necessary for this purpose. Experiments conducted with a solid plate of length $L/3 = 0.18L_s = 16.3\,\text{cm}$ (not presented, see Dupuis et al., 2025) and associated with a E-number of 0.04 proved to be not sufficient to cancel the incoming turbulent shear stress. The latter was only reduced to 50%, compared to the 80% achieved with the present plate. Moreover, the large-scale structures and the associated spatial correlation were hardly affected by the short solid plate of length $L/3$.

The influence of the lateral position of the plate was not assessed in the present study. Yet, Ziada and Rockwell (1982), who investigated the impingement of a Kelvin–Helmholtz vortex street against an edge in the context of noise generation, put forwards the sensitivity of the flow to the lateral offset between the vortex street and the edge. In the present case, the flow behaviour may change if the vortex cores are forced to pass on the low-speed side of the plates, where the boundary layer vorticity alongside the plate is of opposite sign.

CRediT authorship contribution statement

Victor Dupuis: Writing – original draft, Writing – review & editing, Methodology, Data curation, Formal analysis, Conceptualization. **Guillaume Bonduelle:** Data curation, Formal analysis. **Olivier Eiff:** Supervision, Writing – review & editing.

Declaration of competing interest

The authors declare that they have no known competing financial interests or personal relationships that could have appeared to influence the work reported in this paper.

Acknowledgements

We are grateful to D. Groß, M. Ziegler and J. Ulrich for helping with the experimental set-up. We thank F. Kaptur for building a machine for manufacturing the particles used for the LS-PIV. GB received an Erasmus+ grant for traineeship mobilities.

Data availability

Data will be made available on request.

References

Bernal, L., Roshko, A., 1986. Streamwise vortex structure in plane mixing layers. J. Fluid Mech. 170, 499–525.

Bouchez, J., Lajeunesse, E., Gaillardet, J., France-Lanord, C., Dutra-Maia, P., Maurice, L., 2010. Turbulent mixing in the amazon river: The isotopic memory of confluences. Earth Planet. Sci. Lett. 290 (1–2), 37–43.

Branß, T., Aberle, J., 2022. Combined effect of a mobile bed and floodplain edge vegetation on compound channel conveyance. J. Hydraul. Res. 60 (5), 826–834.

Chan, C., Örlü, R., Schlatter, P., Chin, R., 2022. Large-scale and small-scale contribution to the skin friction reduction in a modified turbulent boundary layer by a large-eddy break-up device. Phys. Rev. Fluids 7 (3), 034601.

Cousteix, J., Coustols, E., Arnal, D., 1989. Contrôle et modification de la turbulence. In: Fluid Dynamics of Three-Dimensional Turbulent Shear Flows and Transition, Agard conference proceeding.

Dowling, A., 1985. The effect of large-eddy breakup devices on oncoming vorticity. J. Fluid Mech. 160, 447–463.

Dupuis, V., Eiff, O., Bonduelle, G., 2025. Effect of a streamwise-oriented plate on the shear layer in a compound open-channel flow. In: Conference River Flow 2024, Liverpool. CRC Press, pp. 373–380.

Dupuis, V., Moulin, F.Y., Eiff, O., 2023a. Interaction between a rough bed and an adjacent smooth bed in open-channel flow. J. Fluid Mech. 969, A32.

Dupuis, V., Proust, S., Berni, C., Paquier, A., 2017. Mixing layer development in compound channel flows with submerged and emergent rigid vegetation over the floodplains. Exp. Fluids 58 (4), 30.

Dupuis, V., Schraen, L., Eiff, O., 2023b. Shear layers in two-stage compound channels investigated with LS-PIV. Exp. Fluids 64 (2), 24.

Dupuis, V., Trevisson, M., Wunder, S., McLelland, S., Moulin, F.Y., Chagot, L., Eiff, O., 2023c. Effect of a canopy patch made of streamwise-oriented plates on turbulence in an open-channel flow. Environ. Fluid Mech. 23 (6), 1341–1357.

Epps, B., 2017. Review of vortex identification methods. In: 55th AIAA Aerospace Sciences Meeting. p. 0989.

Fernandes, J.N., Leal, J.B., Cardoso, A.H., 2018. Influence of floodplain and riparian vegetation in the conveyance and structure of turbulent flow in compound channels. In: E3S Web of Conferences, vol. 40, EDP Sciences, p. 06035.

Fouras, A., Soria, J., 1998. Accuracy of out-of-plane vorticity measurements derived from in-plane velocity field data. Exp. Fluids 25, 409–430.

Ghisalberti, M., Nepf, H., 2006. The structure of the shear layer in flows over rigid and flexible canopies. Environ. Fluid Mech. 6 (3), 277–301.

Guezennec, Y., Nagib, H., 1990. Mechanisms leading to net drag reduction in manipulated turbulent boundary layers. AIAA J. 28 (2), 245–252.

Gymnopoulos, M., Ricardo, A.M., Alves, E., Ferreira, R.M., 2019. A circular cylinder in the main-channel/floodplain interface of a compound channel: Effect of the shear flow on drag and lift. J. Hydraul. Res..

Iuso, G., Onorato, M., 1995. Turbulent boundary layer manipulation by outer-layer devices. Meccanica 30, 359–376.

Loehrke, R.I., Nagib, H.M., 1976. Control of free-stream turbulence by means of honeycombs: A balance between suppression and generation. J. Fluids Eng. (ISSN: 0098-2202) 98 (3), 342–351.

Mehta, R., Westphal, R., 1986. Near-field turbulence properties of single-and two-stream plane mixing layers. Exp. Fluids 4 (5), 257–266.

Myers, W., Lyness, J., Cassells, J., 2001. Influence of boundary roughness on velocity and discharge in compound river channels. J. Hydraul. Res. 39 (3), 311–319.

Proust, S., Fernandes, J.N., Leal, J.B., Rivière, N., Peltier, Y., 2017. Mixing layer and coherent structures in compound channel flows: Effects of transverse flow, velocity ratio, and vertical confinement. Water Resour. Res. 53 (4), 3387–3406.

Savill, A., Mumford, J., 1988. Manipulation of turbulent boundary layers by outer-layer devices: skin-friction and flow-visualization results. J. Fluid Mech. 191, 389–418.

Sun, X., Shiono, K., 2009. Flow resistance of one-line emergent vegetation along the floodplain edge of a compound open channel. Adv. Water Resour. 32 (3), 430–438.

Swirydczuk, J., Wilder, M.C., Telionis, D.P., 1993. The interaction of coherent vortices with short flat plates. J. Fluids Eng. 115.

Terrier, B., Robinson, S., Shiono, K., Paquier, A., Ishigaki, T., 2010. Influence of vegetation to boundary shear stress in open channel for overbank flow. In: River Flow, vol. 2010, pp. 285–292.

White, F.M., 1991. Viscous fluid flow. McGraw-Hill.

Wygnanski, I., Fiedler, H., 1970. The two-dimensional mixing region. J. Fluid Mech. 41 (02), 327–361.

Yajnik, K., Acharya, M., 1977. Non-equilibrium effects in a turbulent boundary layer due to the destruction of large eddies. In: Structure and Mechanisms of Turbulence I: Proceedings of the Symposium on Turbulence Held At the Technische Universitä Berlin, August 1–5, 1977. Springer, pp. 249–260.

Ziada, S., Rockwell, D., 1982. Vortex–leading-edge interaction. J. Fluid Mech. 118, 79–107.